

Acoustic Radiation Force-Induced Longitudinal Shear Wave for Ultrasound-based Viscoelastic Evaluation

Hsiao-Chuan Liu^{1,2,§,*}, Hyoung-Ki Lee³, Matthew W. Urban⁴, Qifa Zhou^{1,5}, and Piotr Kijanka^{6,§,*}

¹Department of Ophthalmology, Keck School of Medicine, University of Southern California, Los Angeles, CA, 90033, USA; ²Department of Mechanical Engineering, Massachusetts Institute of Technology, Boston, MA, 02139, USA; ³Philips Inc., San Diego, USA; ⁴Department of Radiology, Mayo Clinic, Rochester, MN, 55905, USA; ⁵Department of Biomedical Engineering, University of Southern California, Los Angeles, CA, 90033, USA ⁶Department of Robotics and Mechatronics, AGH University of Krakow, Krakow, 30059, Poland

§These authors contributed equally to this work. *Corresponding authors

Abstract: Acoustic radiation force (ARF) is widely used to induce shear waves for evaluating the mechanical properties of biological tissues. Two shear waves can be generated when exciting with ARF: a transverse shear wave, also simply called shear wave (SW), and a longitudinal shear wave (LSW). Shear waves (SWs) have been broadly used to assess the mechanical properties. Some articles have reported that the LSW can be used to evaluate mechanical properties locally. However, existing LSW studies are mainly focused on the group velocity evaluation using optical coherence tomography (OCT). Here, we report that a LSW generated with ARF can be used to probe viscoelastic properties, including shear modulus and viscosity, using ultrasound. We took advantage of the surface boundary effect to reflect the LSW, named RLSW, to address the energy deficiency of LSW induced by ARF. We systematically evaluated the experiments with tissue-mimicking viscoelastic phantoms and validated by numerical simulations. Phase velocity and dispersion comparison between the results induced by a RLSW and a SW exhibit good agreement in both the numerical simulations and experimental results. The Kelvin-Voigt (KV) model was used to determine the shear modulus and viscosity. RLSW shows great potential to evaluate localized viscoelastic properties, which could benefit various biomedical applications such as evaluating the viscoelasticity of heterogeneous materials or microscopic lesions of tissues.

Keywords: longitudinal shear wave, acoustic radiation force, viscoelasticity, shear modulus, loss modulus, Kelvin-Voigt, local mechanical property, ultrasound

Introduction

Traditional ultrasound imaging primarily focuses on providing anatomical details [1-3] and blood flow information [4-7]. However, there has been a growing demand for imaging modalities that offer functional and quantitative assessments of tissue characteristics. Ultrasound shear wave elastography (SWE) has emerged as a non-invasive imaging technique that holds great promise in the field of medical diagnostics [8-10]. At the core of SWE is the generation and measurement of shear waves induced by acoustic radiation force (ARF) [11]. This involves the emission of short bursts of focused ultrasound energy, which leads to the creation of transverse shear waves, also simply called a shear wave (SW), traveling within the tissue. The velocity of shear wave propagation is directly related to the mechanical properties of the tissue with stiffer tissues allowing faster wave transmission. As an integral component of elastography, SWE can provide clinicians with valuable insights into pathological conditions across various anatomical regions such as the musculoskeletal system [12-14], liver [15, 16], arteries [17], breast [18, 19], kidney [20], spleen [16], thyroid [21, 22], intervertebral discs [23], and so on. Although SWE has been maturely used in clinics, it requires a certain transverse distance, approximate 5-30 mm assuming using a linear array for example, to allow shear waves to travel, which could be challenging to evaluate mechanical properties locally.

After the induction of ARF, another shear wave is simultaneously generated named the longitudinal shear wave (LSW), distinct from the SW. LSW has garnered increasing attention in the past few years for evaluating local stiffness in tissue-mimicking phantoms [24-27] and *ex-vivo* brain tissues [28, 29]. The LSW is coaxial with the source of the shear wave and exhibits a longitudinal displacement of particles to form waves parallel to the propagation direction with shear wave speed along the thickness of the material after ARF excitation is provided [24, 30]. As the ARF was exerted on the position that is close to the surface of materials, LSW travels outwards on the surface as well as a wave that travels through the thickness of the material, which allows evaluation of localized elasticity through depth by its velocity. Most LSW studies are limited in providing group velocity information to approximately evaluate the stiffness or Young's modulus E using a well-known equation $E = 3\rho c^2$, where ρ is tissue density (usually assumed as 1,000 kg/m³ for tissue-mimicking phantoms/biological tissues), and c is shear wave velocity [24, 25, 28, 29]. Additionally, most LSW studies need to be carried out with an optical coherence tomography (OCT) system which may restrict the use to *ex-vivo* applications due to the shallow penetration with merely a few millimeters depth [25, 28, 29]. Ultrasound transient elastography (TE) is another method to access local stiffness in tissues (most studies are in livers) utilizing a low-frequency external vibrator such as 50 Hz, for example, to generate shear waves [31-34]. The phase velocity of the LSW depends on the distance from the source. Due to the low-frequency excitation with the piston push, the shear wave has enough energy to be able to travel in a much deeper region compared with the ARF excitation, which could increase the spatial and temporal information for frequency-wavenumber analysis. However, the probe used for TE requires a special design embedded with a small piston for mechanical excitations rather than regular linear arrays, which may be limited in some healthcare settings [30].

In the study, we first demonstrate the feasibility of evaluating viscoelasticity including shear modulus and viscosity using an ARF-induced LSW generated by an ultrasound system equipped with a commercial linear array. A direct LSW represents a different strain field from a SW because of polarized longitudinal displacements in the axial direction [26], which makes the direct LSW's momentum transfer efficiency difference from regular SWs. Therefore, the direct LSW carries weak energy making it difficult to travel further in depth. On the contrary, the energy of the reflected LSW comes from the restoring force. As the particles are very close to each other, elastic springs representing interelement forces can be assumed to exist between particles based on the Hooke's law. Once an ARF is generated to push particles downward at the push moment, it can be imagined that all the springs are squeezed. After that, most of the push energy are immediately bounced back by restoring force due to springs released. This restoring force would be smaller than the push force, but still strong. As these restoring forces reach to the surface boundary of a transducer, a strong reflected LSW can be generated caused by a phase change [24, 29]. Systematic studies involving numerical simulations and tissue-mimicking phantoms with various viscosities have been conducted. To assess viscoelasticity, the RLSWs were transformed into the frequency domain using a two-dimensional Fourier transform (2D-FT) to calculate k -space and dispersion relations. The Kelvin-Voigt (KV) model was employed to evaluate viscoelastic properties of materials. Experimental results were compared with transverse SW results and numerical simulations. Due to the advantages of ultrasound, the RLSW can be detected up to 40 mm beneath the surface in our studies, compared with the method using an optical system.

Materials and Methods

Numerical Viscoelastic Phantoms Simulations

The Staggered Grid Finite Difference (SGFD) method was employed to simulate the propagation of mechanical waves in viscoelastic tissue-like materials [35]. The dimensions of the simulated domain were set as $x = 0-40$ mm in the lateral direction and $z = 0-50$ mm in the axial direction. Air-solid boundary

conditions were applied to the upper surface of the phantom, while the modeled region on both sides and the bottom of the phantom was enclosed by a 60 mm wide perfectly matched layer (PML) area [35]. The entire model was discretized into sufficiently small square cells with grid dimensions $\Delta x = \Delta z = 0.1$ mm. The time step for the simulations was determined based on the Courant–Friedrichs–Lewy (CFL) condition. The CFL condition was applied to the resultant wave speed of both the shear and compressional waves propagating in the model as $CFL = \frac{\Delta t}{\Delta x} * \sqrt{V_s^2 + V_c^2}$, where V_s is the shear wave speed and V_c is the compressional wave speed. Δt and Δx are the time step and spatial grid dimension, respectively. To ensure numerical stability, the CFL value was set to 0.5 [36]. To induce propagating shear waves, an ARF push beam was utilized [35]. The ARF push beam was centered at a focal depth of 10 mm and was applied for a duration of 50 μ s. Then, the particle velocity shear wave motion data were measured in the lateral and axial directions. The tissue-mimicking viscoelastic models have a constant shear modulus (μ_1) of 8.33 kPa, resulting in a shear wave speed of 2.8 m/s. A varying shear viscosity (μ_2) was employed, ranging from 0.05 to 2.5 Pa·s. Models with a higher μ_2/μ_1 ratio are considered more viscoelastic. The mass density, ρ , of the models is 1,000 kg/m³, and the Poisson's ratio corresponds to the compressional wave speed of 1500 m/s. The velocity wavefield was sampled at a rate of 10 kHz and used for further data processing. The computational methodology was executed using MATLAB R2023a release (MathWorks, Natick, MA, USA) software, which utilized parallel computation technology and the capabilities of modern Graphics Processing Units (GPUs) and the Compute Unified Device Architecture (CUDA) present in cost-effective graphical cards. Simulations took approximately 110 minutes per model using NVIDIA GeForce RTX 4090 and software MATLAB implementations.

Systematic Experiments on Tissue-Mimicking Viscoelastic Materials

In our experiments, three custom-made tissue-mimicking viscoelastic phantoms (CIRS Inc., Norfolk, VA, USA, manufactured between 2017 and 2018) were employed to assess the feasibility of measuring longitudinal shear wave attenuation. The reference mechanical properties of these phantoms are currently unknown. Data acquisition was carried out using a programmable ultrasound system (V1, Verasonics Inc., Kirkland, WA). The ARF push beams were generated using a linear array transducer (L7-4, Philips Healthcare, Andover, MA) with a focal point set at 10 mm under the surface of the phantoms. The push duration was set as 400 μ s, and the frequency for ARF push was 4.09 MHz. The ARF push beam was constructed using 64 active central elements of the L7-4 probe, which corresponds to F#/0.5. To capture the shear wave propagation, we performed plane wave compounding (PWC) [37]. The tracking beam had a center frequency of 5 MHz (i.e., $\lambda = 0.308$ mm) and its pulse repetition frequency (PRF) was 12.5 kHz. PWC excited all transducer elements with three angles $[-4^\circ, 0^\circ, 4^\circ]$ without transmit apodization. The frame rate of both PWC was increased to the PRF using the time-aligned PWC (TAPWC) method on the acquired IQ data [38]. To obtain motion data, we calculated the time delay between IQ data of two consecutive compounded images, which corresponds to the particle velocity profile (i.e., the time derivative of the displacement profile). A 1-D autocorrelation method (Kasai method) was used as a time-delay estimation algorithm with the kernel size of 3λ [39]. No filtering was applied to the motion data unless otherwise stated. The final motion data were 268×256 spatial pixels (with the axial and lateral spatial resolution of 0.148 and 0.149 mm, respectively) and 111 frames in time.

Each phantom underwent ten successive shear wave acquisitions at various spatial positions.

Viscoelastic Parameters Estimation

The viscoelastic parameters were determined for both numerical and CIRS commercial tissue mimicking viscoelastic phantoms. In materials with viscoelastic properties, the shear modulus is frequency dependent and can be characterized with the complex shear modulus, $G^*(\omega)$, defined as

$$G^*(\omega) = G_S(\omega) + iG_L(\omega), \quad (1)$$

where ω is the angular frequency ($2\pi f$), $G_S(\omega)$ is storage modulus and $G_L(\omega)$ is loss modulus [40, 41]. The complex shear modulus can also be written as

$$G^*(\omega) = \frac{\rho\omega^2}{k^2(\omega)}, \quad (2)$$

where ρ is the mass density of the medium and usually assumed to be 1,000 kg/m³ for the soft tissue. The variable k is the complex wavenumber and can be written as $k(\omega) = k_1(\omega) + ik_2(\omega)$. To thoroughly describe the viscoelastic properties of materials, the KV rheological model [35] was adopted to analyze dispersion curves in an f-k map created by a two-dimensional Fourier transform (2D-FT) of a spatiotemporal particle motion with the wavenumber-frequency pairs [42, 43]. The shear wave phase velocity, C_p , can be extracted from finding the peaks in the f-k distribution along a given search direction and written as

$$C_p(\omega) = \frac{\omega}{\text{Re}[k(\omega)]} = \frac{\omega}{k_1(\omega)}. \quad (3)$$

The KV model consists of a viscous damper in parallel to an elastic spring. The elastic spring contributes the property of shear modulus (μ_1) and the viscous damper provides viscosity (μ_2). To apply this model, the medium is assumed to be isotropic and locally homogeneous, and then $G_S(\omega) = \mu_1$ and $G_L(\omega) = \omega\mu_2$. A nonlinear least-squares fit method (*lsqcurvefit*) was utilized to estimate the $G_S(\omega)$ and $G_L(\omega)$. The complete viscoelastic shear modulus of the KV model, $\mu^*(\omega)$, can be written as

$$\mu^*(\omega) = \mu_1 + i\omega\mu_2. \quad (4)$$

Substituting equation (4) into (2) and working through equation (3), the shear wave phase velocity for the KV model (C_{KV}) can be written as

$$C_{KV}(\omega) = \frac{\sqrt{2(\mu_1^2 + \omega^2\mu_2^2)}}{\rho(\mu_1 + \sqrt{\mu_1^2 + \omega^2\mu_2^2})}. \quad (5)$$

To estimate the parameters μ_1 and μ_2 , a nonlinear least-squares problem (NLSQ) was solved for $V_{KV}(\omega)$ in the following form

$$[\mu_1, \mu_2] = \min_{\mu_1, \mu_2} \|C_{KV}(f) - C_{2DFT}(f)\|_2^2, \quad (6)$$

where V_{2DFT} corresponds to the phase velocity extracted from the measured shear wave motion. The KV fit was done using various frequency ranges for different phantoms. The frequency ranges were predefined based on the f-k distribution. The frequency ranges from 100 Hz to the cut-off frequency of 1000, 750, 600, 550, 500, and 500 Hz for phantoms with viscosities from 0.02 to 2.5 Pa·s, respectively, were selected to calculate μ_1 and μ_2 for all numerical phantoms. Viscoelastic parameters estimation was performed using two types of shear wave motion data: the RLSW propagating in the axial direction and the conventional SW propagating in the lateral direction. The results obtained for the SW validated the results obtained with the RLSW. The full details of the viscoelastic modeling can be found in our previous papers [40, 44, 45].

Results

Numerical Simulation Results

Figure 1 shows a numerical simulation of an RLSW induced by the ARF push to generate particle motions. Particle velocity motion data in the lateral and axial distances for four subsequent time points (0, 1, 3, and 5 ms) are displayed. The snapshot at 0 ms shows the ARF push beam focused at 10 mm in the z-direction and 20 mm in the x-direction, respectively (Fig. 1a). Figure 1b presents that SW and RLSW are generated and propagating in the lateral direction (SW, purple arrow) and in the axial directions (RLSW, blue arrow),

illustrated in Fig. 1c. Fire 1d shows the same SW and RLSW continuously propagating further toward the x and z directions, respectively. In addition, the time W propagating from the surface was also generated, observed at time of 5 ms (dark blue arrow). The stronger energy of the RLSW can be observed compared with the LSW generated from the original focal point. In this work, we focused on the RLSW for characterizing the viscoelastic properties of the examined numerical and experimental phantoms.

The shear wave particle velocity motion data with various viscosity values for numerical viscoelastic phantoms were analyzed. Figure 2 illustrates spatiotemporal data for SWs (top row) and RLSWs (bottom row) with variety of viscoelastic properties from 0.05 Pa·s (control) (Fig. 2a) to 2.5 Pa·s (Fig. 2f). In the case of the SW, two shear waves are observed propagating in opposite directions along the lateral distance. Conversely, the RLSWs in the bottom row of Fig. 2 exhibit a distinct behavior. Two waveforms are visible in these plots. One waveform propagates downwards from 10 mm (ARF focal point) along the axial distance, while the other originates from 10 mm upwards, reaches the top surface, reflects from the rigid boundary, and subsequently travels down the phantom. However, faster attenuation with higher viscosity can be observed in both SWs and RLSWs.

Figure 3 shows the f-k distribution with various viscosity values reconstructed from the spatiotemporal data in Fig. 1. The f-k maps are normalized by the maximum wavenumber in the frequency direction for each frequency. The f-k distribution of SWs covers a broader frequency band that can extend to 1000 Hz, compared to those of RLSWs, particularly for varying viscosity values where the f-k distribution of RLSW shortens with the frequency band ranges from 800 Hz to 500 Hz as viscosity increases. In the phase velocity analysis, phase velocities of SWs and RLSWs were extracted from these f-k maps and compared with analytical results (C_{KV}) presented in Fig. 4 (dark solid lines). As previously observed for the f-k maps, the narrower frequency band for RLSWs, compared with the SWs (blue circles), is observed through the limited bandwidth for the measured phase velocities, presented in Fig. 4 (red dots). However, a consistent result of phase velocities was observed between the analytical results and those measured based on SW and RLSW waves. The phase velocity curves calculated in Fig. 4 were then used to estimate the viscoelastic parameters, and the results are summarized in Table I. The shear modulus and viscosity estimates obtained based on RLSW showed good agreement with those using SW. However, shear modulus estimates were slightly underestimated for using both SW and RLSWs.

Systematic Experimental Studies in Tissue-mimicking Viscoelastic Phantoms

Experimental studies in the custom-made tissue-mimicking phantoms with three different viscosities were conducted to measure the SW and RLSW velocities. Spatiotemporal shear wave particle velocity signals of three viscoelastic phantoms described in Section 2.2. are shown in Figure 5 as an example. Five acquisitions were conducted in each phantom. Two types of waves including SWs and RLSWs can be observed. The mean group velocity values of SW were in the range of 2.58 ± 0.01 m/s, 3.35 ± 0.02 m/s, and 4.70 ± 0.01 m/s, presented in Fig. 5a-c. The corresponding RLSW with the group velocity of 2.49 m/s, 3.25 m/s and 4.63 m/s were shown in Fig. 5d-f, respectively. The mean group velocity values of RLSW were in the range of 2.57 ± 0.13 m/s, 3.41 ± 0.06 m/s, and 4.75 ± 0.12 m/s. The group velocities of the RLSW show a highly consistent results with those of the SW.

The f-k distribution maps of three commercial viscoelastic phantoms, normalized by the wavenumber maxima, were shown in Figs. 6a-c for the SW and in Figs. 6d-f for the RLSW. Similar to the numerical simulation results, a narrower frequency band was observed for the RLSW experimental measurements, especially in the higher viscosity case. For a frequency reaching approximately 600 Hz, the f-k maps show more noise for the RLSW (Figs. 6d-f) compared to the SW (Figs. 6a-c). This phenomenon is visible for all tested phantoms. The f-k maps phase velocity dispersion curves were calculated and presented in Figs. 6g-

i. A good overlap between the results for SW and RLSW was obtained. The mean phase velocity and standard deviation of SW within the frequency ranges from 200 Hz to 600 Hz in three phantoms were 2.55 ± 0.14 m/s, 3.36 ± 0.14 m/s, and 4.61 ± 0.33 m/s. Comparing with the RLSW, the mean phase velocity and standard deviation were 2.67 ± 0.13 m/s, 3.39 ± 0.18 m/s, and 4.67 ± 0.29 m/s. The phase velocities of the RLSW are in good agreement with those of the SW. Higher variation was also observed for frequencies above 600 Hz, which could be caused by the increased noise in the f-k maps.

The calculated phase velocity curves of the SW and the RLSW were used to estimate the viscoelastic properties of the phantoms using a KV fit in the frequency range of 300-500 Hz (Fig. 7). Figure 7 exhibits the calculated storage modulus $G_S(\omega)$ and loss modulus $G_L(\omega)$ in three viscoelastic phantoms by using the KV model. The dispersion for each acquisition was fit for individual storage and modulus estimates. The blue and red lines represent viscoelastic properties of the three viscoelastic phantoms by using SW and the RLSW, respectively. The solid and circled lines depict the $G_S(\omega)$ and $G_L(\omega)$, respectively. Table 2 shows the summary of the estimated shear modulus and loss modulus properties with standard deviations of the three viscoelastic phantoms. A good agreement for the storage modulus and loss modulus were obtained between the SW and LSW data for all viscoelastic phantoms. The viscoelastic properties using the RLSW are positively correlated with the those using the SW.

Discussion

A method for estimating the shear modulus and shear viscosity in the axial direction was proposed using RLSWs generated by an ARF push beam. This approach involves utilizing shear waves that propagate in the axial direction and are reflected from the top surface. The approach was tested on simulated data from numerical models and experimental data in custom made tissue-mimicking viscoelastic phantoms. The results were generally similar between the SW and RLSW methods. The RLSW method achieved a narrower frequency bandwidth due to high-frequency loss caused by boundary and noise characteristics (compared with simulation without noise), but it was still sufficient to be able to reconstruct the properties of the examined materials (Table 1 and 2).

In the simulation results, it was observed that the shear modulus was slightly underestimated in both SW and RLSW (Table 1). The reason is because the KV fit is sensitive to the frequency range [46] used for the calculations in Eq. (6). The lower the frequency range, the more sensitive the KV fit is to potential noise that may affect the estimates of the two viscoelastic parameters μ_1 and μ_2 . The underestimation of μ_1 was observed because a lower frequency limit of 150 Hz was used, which corresponds to a wavelength of 19.2 mm. The longer the wavelength for lower frequencies, the greater the errors that may appear in the measured phase velocity for the low frequency range which causes bias in the estimated μ_1 parameter.

The proposed approach has several major advantages. RLSW can be generated using the ARF push and no additional transducer other than a phased array probe is required. The RLSW uses a reduced amount of data in the lateral direction. Therefore, it can be used to study tissues in a laterally local perspective. Local mechanical properties of tissues are analyzed in the axial direction, which has great potential in scenarios where local viscoelastic properties of tissues in the axial direction are required as a point measurement method, such as to explore microscopic abnormalities and residual lesions identified in neuroscience [47].

Another advantage is that the RLSW approach uses shear wave velocity waveforms measured in the axial direction (one or a few locations in the lateral direction). Therefore, the temporal resolution of the acquisitions can be increased by activating only a few transducer elements. This, in turn, can increase the signal-to-noise ratio of shear wave tracking. In addition, instead of using plane waves, focused transmit beams could also increase the SNR at the two locations of interest [48].

The ARF push configuration may affect the amplitude of the generated RLSWs. Based on our preliminary comparative studies, it is recommended to use a focused beam with $f\# < 1$ rather than a wide beam with $f\# \geq 1$ [49]. A focused beam with $f\# < 1$ with focus that is close to the surface (such as 10 mm under the surface) can ensure the most energy can be reflected by the boundary and RLSWs can propagate further in axial direction. Extensive research on this aspect was beyond the main purpose of this work and is planned for the future study.

There are a few limitations of this method. First, the extent of penetration may be limited for the propagation of the RLSW, compared with SWs. Second, due to representing a different strain field from conventional SW, the energy of the RLSW would be weaker than it of the conventional SWs, which implies that the temporal and spatial distance could be limited so that the signals in high frequency regions would present some noise, resulting in lower SNR. Additionally, relevant clinical applications would be more specific such as neurology, tissue engineering or material science. In this study, there could be difficulty for focusing close to the surface of objects using a linear array transducer. However, it can be solved by using a single element needle transducer to produce ARF pushes [50]. The ultrasound longitudinal shear wave shows a promising method to estimate localized viscoelastic properties. In future work, we will use this method to evaluate viscoelasticity of biological tissues using the proposed RLSW method.

Conclusions

This work demonstrates the use of acoustic radiation force generated longitudinal shear waves to axially evaluate localized viscoelastic properties, including shear modulus and shear viscosity. The method was investigated on numerical viscoelastic phantoms and custom-made viscoelastic phantom data. Compared to conventional shear wave measurements, longitudinal shear waves produced comparable results in terms of phase velocity dispersion curves and estimated KV viscoelastic parameters. More importantly, longitudinal shear waves can provide information about the mechanical properties of a tissue in a localized lateral position.

Acknowledgements

This work was supported by the National Institutes of Health (NIH) R03EB032958, R21GM154167 and in part by the National Science Center in Poland under research project no. UMO–2021/43/D/ST8/01295. The content is solely the responsibility of authors and does not necessarily represent the official views of the NIH.

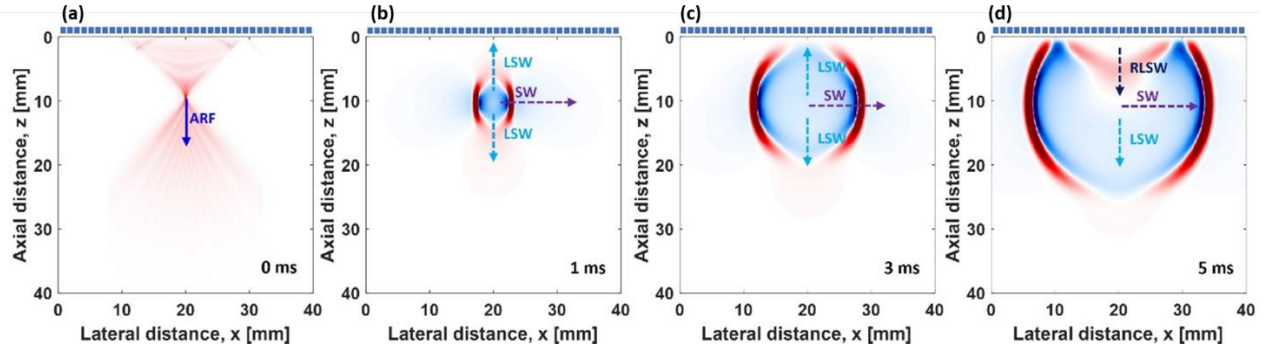


Figure 1: (a) An illustration of the numerical simulation result shows ARF-induced LSW. The LSW travels at (b) 1 ms and (c) 3 ms in the axial directions. (d) The reflected LSW (RLSW) can be observed, which is generated by the surface boundary.

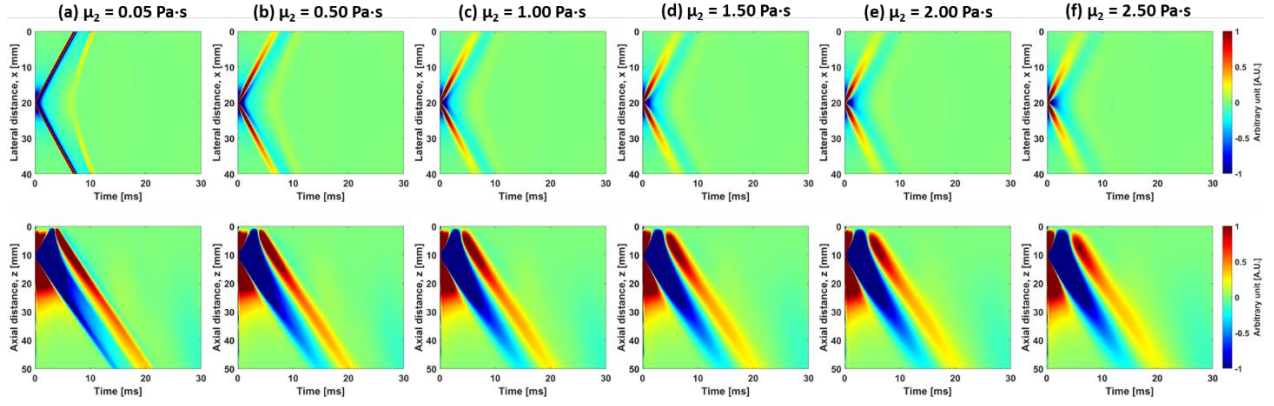


Figure 2: Particle velocity wave motion data for the SW propagating in the lateral direction (top row), and the RLSW propagating in the axial direction. The results display the numerical tissue-mimicking materials for various viscosity values ranging from (a) 0.05 Pa·s (control), (b) 0.50 Pa·s, (c) 1.00 Pa·s, (d) 1.50 Pa·s, (e) 2.00 Pa·s to (f) 2.50 Pa·s.

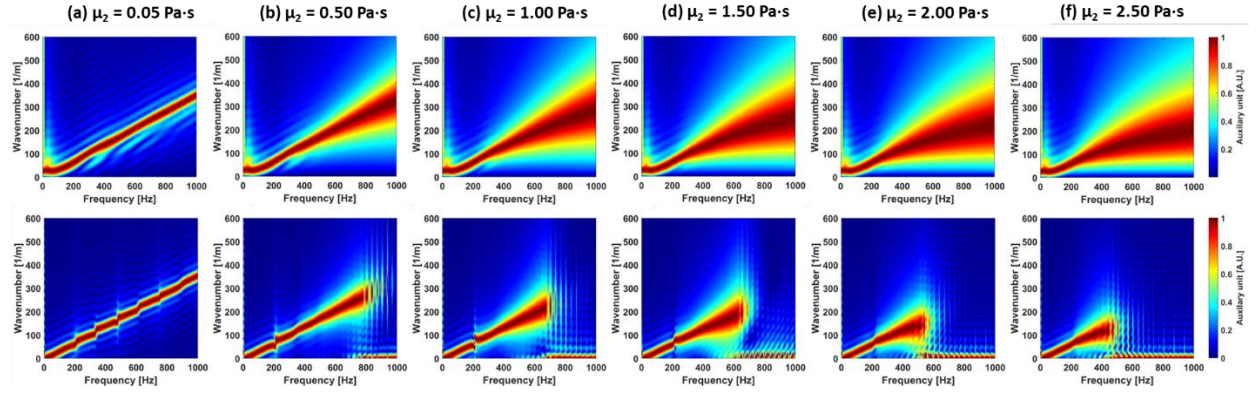


Figure 3: The frequency-wavenumber spectrum calculated for SW propagating in the lateral direction (top row), and the RLSW propagating in the axial direction (bottom row). The f-k maps are normalized by wavenumber maxima in the frequency direction for each frequency. The results display the numerical tissue-mimicking materials for various viscosity values ranging from (a) 0.05 Pa·s (control), (b) 0.50 Pa·s, (c) 1.00 Pa·s, (d) 1.50 Pa·s, (e) 2.00 Pa·s to (f) 2.50 Pa·s. There are breaks happen around 200Hz, which is caused by a discontinuous area of the energy distribution in k-space before the normalization.

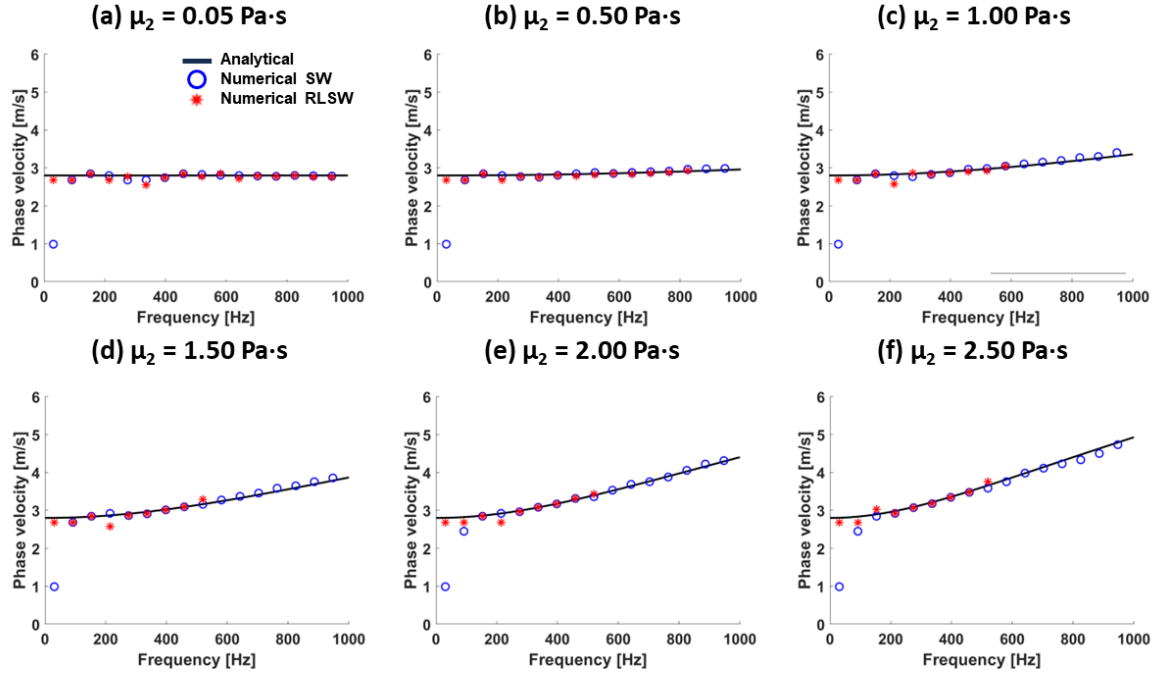


Figure 4. Phase velocity dispersion curves calculated for the numerical tissue-mimicking phantoms for shear waves (SW) propagating in the lateral direction (blue circles), and the RLSW propagating in the axial direction (red stars). The results were calculated for various viscosity values ranging (a) 0.05 Pa·s (control), (b) 0.50 Pa·s, (c) 1.00 Pa·s, (d) 1.50 Pa·s, (e) 2.00 Pa·s to (f) 2.50 Pa·s.

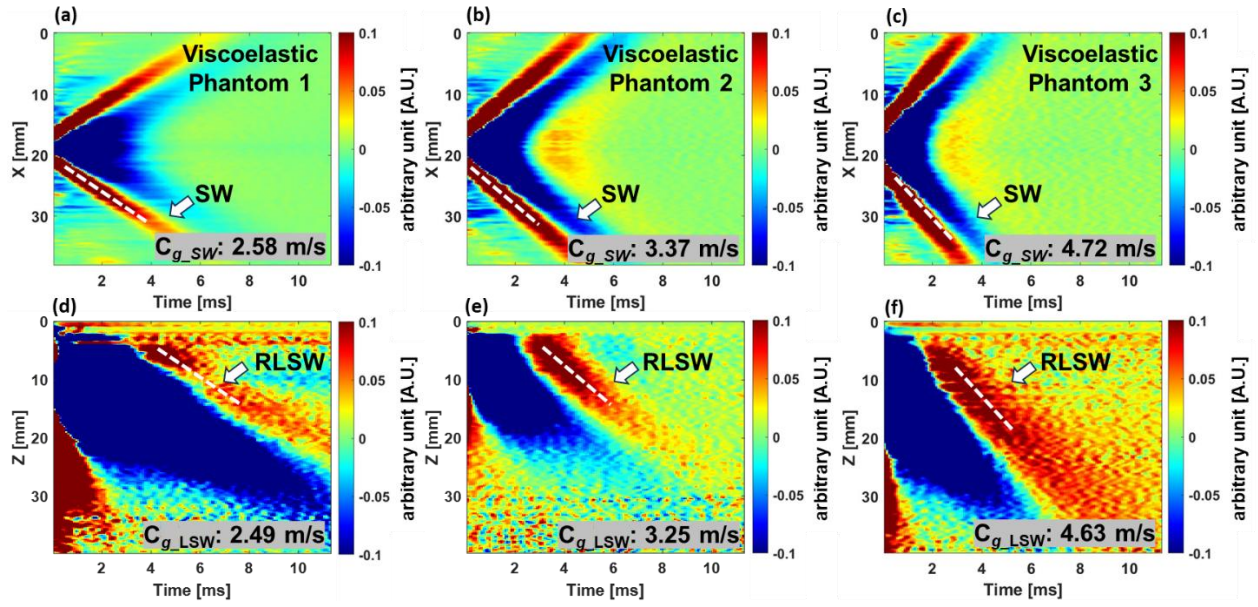


Figure 5: Particle velocity wave motion data from the three tissue-mimicking CIRS commercial viscoelastic phantoms were calculated for (a-c) SW propagating in the lateral direction, and (d-f) the RLSW propagating in the axial direction. The group velocities of the RLSWs in the three phantoms are a good agreement with those of the SWs.

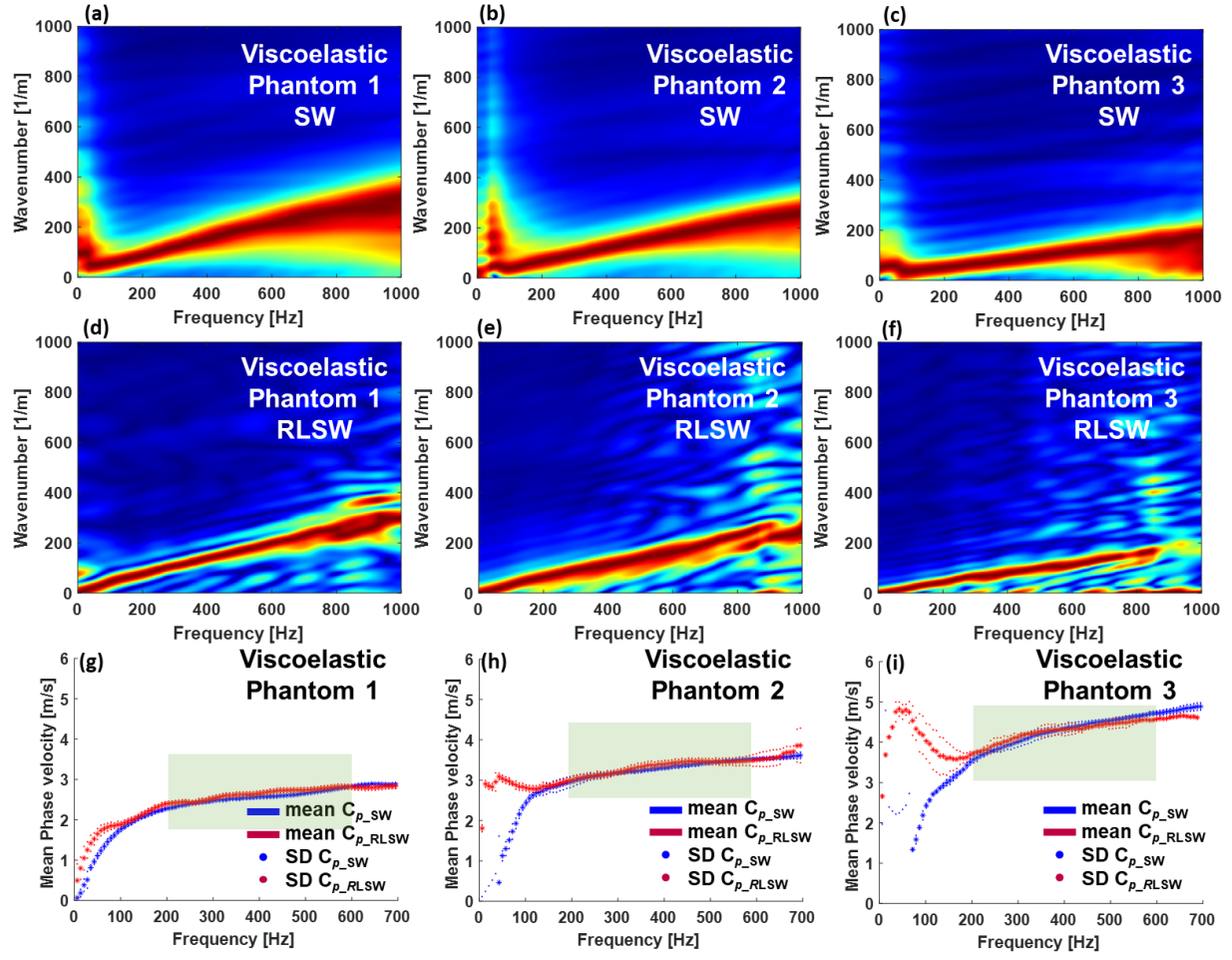


Figure 6: (a-c) The frequency-wavenumber spectrum calculated for SW propagating in the lateral direction in three commercial viscoelastic phantoms, and (d-f) RLSW propagating in the axial direction in three commercial viscoelastic phantoms. The f-k maps are normalized by wavenumber maxima in the frequency direction. (g-i) Mean phase velocity dispersion curves ($n = 5$) were calculated for SW propagating in the lateral direction (blue), and RLSW propagating in the axial direction (red) with the frequency ranges from 200 Hz to 600 Hz in the three commercial viscoelastic phantoms.

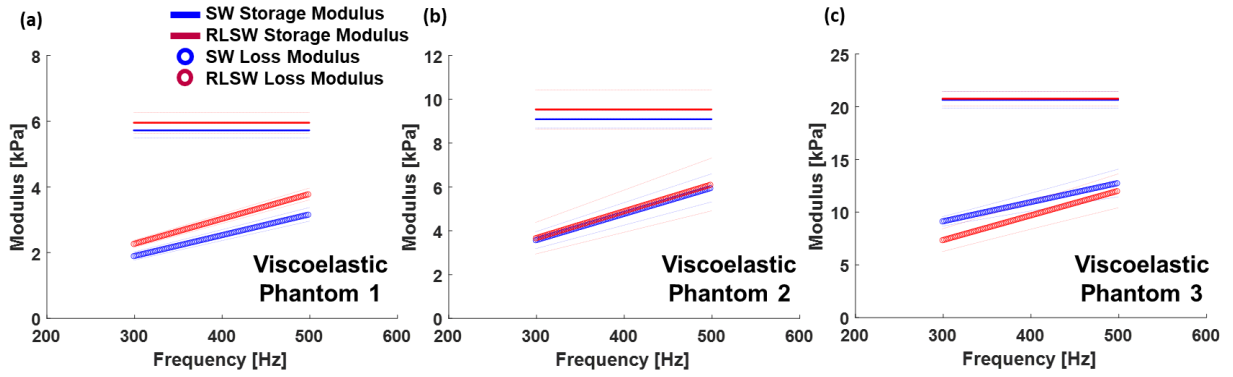


Figure 7. (a-c) The KV model was used to estimate storage modulus and loss modulus of the RLSW in the three viscoelastic commercial phantoms. A nonlinear least-squares fit method applying to the frequency range from 300 Hz to 500 Hz was performed. The storage modulus and loss modulus of the RLSWs in the three viscoelastic commercial phantoms were in a good agreement with those of the SWs.

Table I. Viscoelastic parameters estimated for shear waves propagating in the lateral direction (SW), and longitudinal shear waves propagating in the axial direction (RLSW). Results were presented for the numerical tissue-mimicking phantoms.

Analytical		Numerical			
		SW		RLSW	
μ_1 [kPa]	μ_2 [Pa·s]	μ_1 [kPa]	μ_2 [Pa·s]	μ_1 [kPa]	μ_2 [Pa·s]
8.33	0.02	7.78	0.01	7.75	0.01
8.33	0.50	7.89	0.50	7.74	0.48
8.33	1.00	7.71	1.09	7.64	1.07
8.33	1.50	7.80	1.53	7.52	1.52
8.33	2.00	7.68	2.05	7.60	2.15
8.33	2.50	7.75	2.51	7.75	2.51

Table II. The mean and standard deviation of the storage and loss moduli calculated for the tissue-mimicking viscoelastic phantoms. Results were calculated within a frequency range of 300-500 Hz. Results are reported in the unit of kPa.

	Phantom 1		Phantom 2		Phantom 3	
	SW	RLSW	SW	RLSW	SW	RLSW
Storage modulus	5.72 ± 0.24	5.95 ± 0.32	9.09 ± 0.40	9.53 ± 0.89	20.66 ± 0.79	20.77 ± 0.67
Loss modulus	2.53 ± 0.16	3.03 ± 0.14	4.76 ± 0.51	4.89 ± 0.96	10.95 ± 0.85	9.68 ± 1.32

References

- [1] E. Landhuis, "Ultrasound for the brain," *Nature*, vol. 551, no. 7679, pp. 257-259, Nov 9 2017, doi: 10.1038/d41586-017-05479-7.
- [2] B. J. Ostrum, B. B. Goldberg, and H. J. Isard, "A-mode ultrasound differentiation of soft-tissue masses," *Radiology*, vol. 88, no. 4, pp. 745-9, Apr 1967, doi: 10.1148/88.4.745.
- [3] R. Bases, "Diagnostic ultrasound," *Science*, vol. 228, no. 4700, pp. 648, 650, May 10 1985, doi: 10.1126/science.228.4700.648-a.
- [4] E. L. Yeh and R. C. Meade, "Pulsed Doppler studies in B-mode ultrasound scanning," *Radiology*, vol. 122, no. 2, pp. 521-2, Feb 1977, doi: 10.1148/122.2.521.
- [5] R. W. Barnes, E. E. Slaymaker, and F. J. Hahn, "Thromboembolic complications of angiography for peripheral arterial disease: prospective assessment by Doppler ultrasound," *Radiology*, vol. 122, no. 2, pp. 459-61, Feb 1977, doi: 10.1148/122.2.459.
- [6] H. S. Sear and M. J. Friedenber, "Angiographic exposure timing by Doppler-shift ultrasound," *Radiology*, vol. 106, no. 3, pp. 631-4, Mar 1973, doi: 10.1148/106.3.631.
- [7] D. L. Franklin, W. Schlegel, and R. F. Rushmer, "Blood flow measured by Doppler frequency shift of back-scattered ultrasound," *Science*, vol. 134, no. 3478, pp. 564-5, Aug 25 1961, doi: 10.1126/science.134.3478.564.
- [8] A. Caenen *et al.*, "Assessing cardiac stiffness using ultrasound shear wave elastography," *Phys Med Biol*, vol. 67, no. 2, Jan 17 2022, doi: 10.1088/1361-6560/ac404d.
- [9] L. J. Brattain, A. Ozturk, B. A. Telfer, M. Dhyani, J. R. Grajo, and A. E. Samir, "Image Processing Pipeline for Liver Fibrosis Classification Using Ultrasound Shear Wave Elastography," *Ultrasound Med Biol*, vol. 46, no. 10, pp. 2667-2676, Oct 2020, doi: 10.1016/j.ultrasmedbio.2020.05.016.
- [10] V. Dutt, R. R. Kinnick, R. Muthupillai, T. E. Oliphant, R. L. Ehman, and J. F. Greenleaf, "Acoustic shear-wave imaging using echo ultrasound compared to magnetic resonance elastography," *Ultrasound Med Biol*, vol. 26, no. 3, pp. 397-403, Mar 2000, doi: 10.1016/s0301-5629(99)00166-0.
- [11] K. Nightingale, S. McAleavey, and G. Trahey, "Shear-wave generation using acoustic radiation force: in vivo and ex vivo results," *Ultrasound Med Biol*, vol. 29, no. 12, pp. 1715-23, Dec 2003, doi: 10.1016/j.ultrasmedbio.2003.08.008.
- [12] N. Iida, A. R. Thoreson, R. L. Reisdorf, I. Tsukamoto, H. El Hor, and C. Zhao, "Relationship Between the Changes of Tendon Elastic Moduli With Ultrasound Shear Wave Elastography and Mechanical Compression Test," *Ultrasound Med Biol*, vol. 50, no. 4, pp. 586-591, Apr 2024, doi: 10.1016/j.ultrasmedbio.2024.01.001.
- [13] M. L. Stiver, S. A. Mirjalili, and A. M. R. Agur, "Measuring Shear Wave Velocity in Adult Skeletal Muscle with Ultrasound 2-D Shear Wave Elastography: A Scoping Review," *Ultrasound Med Biol*, vol. 49, no. 6, pp. 1353-1362, Jun 2023, doi: 10.1016/j.ultrasmedbio.2023.02.005.
- [14] A. Phan, J. Lee, and J. Gao, "Ultrasound shear wave elastography in assessment of skeletal muscle stiffness in senior volunteers," *Clin Imaging*, vol. 58, pp. 22-26, Nov-Dec 2019, doi: 10.1016/j.clinimag.2019.06.006.
- [15] M. Byenfeldt, A. Elvin, and P. Fransson, "On Patient Related Factors and Their Impact on Ultrasound-Based Shear Wave Elastography of the Liver," *Ultrasound Med Biol*, vol. 44, no. 8, pp. 1606-1615, Aug 2018, doi: 10.1016/j.ultrasmedbio.2018.03.031.
- [16] G. Ferraioli *et al.*, "Ultrasound point shear wave elastography assessment of liver and spleen stiffness: effect of training on repeatability of measurements," *Eur Radiol*, vol. 24, no. 6, pp. 1283-9, Jun 2014, doi: 10.1007/s00330-014-3140-y.

- [17] N. R. Hugenberg *et al.*, "Toward improved accuracy in shear wave elastography of arteries through controlling the arterial response to ultrasound perturbation in-silico and in phantoms," *Phys Med Biol*, vol. 66, no. 23, Nov 26 2021, doi: 10.1088/1361-6560/ac38fe.
- [18] A. Evans, Y. T. Sim, B. Lawson, and P. Whelehan, "Audit of eliminating biopsy for presumed fibroadenomas with benign ultrasound greyscale and shear-wave elastography findings in women aged 25-39 years," *Clin Radiol*, vol. 75, no. 11, pp. 880 e1-880 e3, Nov 2020, doi: 10.1016/j.crad.2020.08.002.
- [19] K. Skerl, S. Vinnicombe, E. Giannotti, K. Thomson, and A. Evans, "Influence of region of interest size and ultrasound lesion size on the performance of 2D shear wave elastography (SWE) in solid breast masses," *Clin Radiol*, vol. 70, no. 12, pp. 1421-7, Dec 2015, doi: 10.1016/j.crad.2015.08.010.
- [20] F. Bob *et al.*, "Ultrasound-Based Shear Wave Elastography in the Assessment of Patients with Diabetic Kidney Disease," *Ultrasound Med Biol*, vol. 43, no. 10, pp. 2159-2166, Oct 2017, doi: 10.1016/j.ultrasmedbio.2017.04.019.
- [21] A. C. Lam, S. W. Pang, A. T. Ahuja, and K. S. Bhatia, "The influence of precompression on elasticity of thyroid nodules estimated by ultrasound shear wave elastography," *Eur Radiol*, vol. 26, no. 8, pp. 2845-52, Aug 2016, doi: 10.1007/s00330-015-4108-2.
- [22] K. S. Bhatia, A. C. Lam, S. W. Pang, D. Wang, and A. T. Ahuja, "Feasibility Study of Texture Analysis Using Ultrasound Shear Wave Elastography to Predict Malignancy in Thyroid Nodules," *Ultrasound Med Biol*, vol. 42, no. 7, pp. 1671-80, Jul 2016, doi: 10.1016/j.ultrasmedbio.2016.01.013.
- [23] C. Vergari *et al.*, "Non-invasive biomechanical characterization of intervertebral discs by shear wave ultrasound elastography: a feasibility study," *Eur Radiol*, vol. 24, no. 12, pp. 3210-6, Dec 2014, doi: 10.1007/s00330-014-3382-8.
- [24] H. C. Liu, B. Gaihre, P. Kijanka, L. Lu, and M. W. Urban, "Acoustic Force Elastography Microscopy," *IEEE Trans Biomed Eng*, vol. 70, no. 3, pp. 841-852, Mar 2023, doi: 10.1109/TBME.2022.3203435.
- [25] J. Zhu *et al.*, "Longitudinal shear wave imaging for elasticity mapping using optical coherence elastography," *Appl Phys Lett*, vol. 110, no. 20, p. 201101, May 15 2017, doi: 10.1063/1.4983292.
- [26] S. Catheline and N. Benech, "Longitudinal shear wave and transverse dilatational wave in solids," *J Acoust Soc Am*, vol. 137, no. 2, pp. EL200-5, Feb 2015, doi: 10.1121/1.4907742.
- [27] J. Zhu *et al.*, "Coaxial excitation longitudinal shear wave measurement for quantitative elasticity assessment using phase-resolved optical coherence elastography," *Opt Lett*, vol. 43, no. 10, pp. 2388-2391, May 15 2018, doi: 10.1364/OL.43.002388.
- [28] Y. Zhu *et al.*, "Noncontact longitudinal shear wave imaging for the evaluation of heterogeneous porcine brain biomechanical properties using optical coherence elastography," *Biomed Opt Express*, vol. 14, no. 10, pp. 5113-5126, Oct 1 2023, doi: 10.1364/BOE.497801.
- [29] F. Zvietcovich *et al.*, "Longitudinal shear waves for elastic characterization of tissues in optical coherence elastography," *Biomed Opt Express*, vol. 10, no. 7, pp. 3699-3718, Jul 1 2019, doi: 10.1364/BOE.10.003699.
- [30] J. M. Cormack, Y. H. Chao, B. T. Archer, K. Kim, K. S. Spratt, and M. F. Hamilton, "Focused Shear Wave Beam Propagation in Tissue-Mimicking Phantoms," *IEEE Trans Biomed Eng*, vol. 71, no. 2, pp. 621-630, Feb 2024, doi: 10.1109/TBME.2023.3311688.
- [31] M. Tanter, J. Bercoff, L. Sandrin, and M. Fink, "Ultrafast compound imaging for 2-D motion vector estimation: application to transient elastography," *IEEE Trans Ultrason Ferroelectr Freq Control*, vol. 49, no. 10, pp. 1363-74, Oct 2002, doi: 10.1109/tuffc.2002.1041078.
- [32] L. Sandrin, M. Tanter, J. L. Gennisson, S. Catheline, and M. Fink, "Shear elasticity probe for soft tissues with 1-D transient elastography," *IEEE Trans Ultrason Ferroelectr Freq Control*, vol. 49, no. 4, pp. 436-46, Apr 2002, doi: 10.1109/58.996561.

- [33] L. Sandrin, M. Tanter, S. Catheline, and M. Fink, "Shear modulus imaging with 2-D transient elastography," *IEEE Trans Ultrason Ferroelectr Freq Control*, vol. 49, no. 4, pp. 426-35, Apr 2002, doi: 10.1109/58.996560.
- [34] S. Catheline, J. L. Thomas, F. Wu, and M. A. Fink, "Diffraction field of a low frequency vibrator in soft tissues using transient elastography," *IEEE Trans Ultrason Ferroelectr Freq Control*, vol. 46, no. 4, pp. 1013-9, 1999, doi: 10.1109/58.775668.
- [35] M. Osika and P. Kijanka, "Ultrasound Shear Wave Propagation Modeling in General Tissue-Like Viscoelastic Materials," *Ultrasound Med Biol*, vol. 50, no. 4, pp. 627-638, Apr 2024, doi: 10.1016/j.ultrasmedbio.2024.01.008.
- [36] J. C. Strikwerda, *Finite Difference Schemes and Partial Differential Equations*. Society for Industrial and Applied Mathematics, 2004.
- [37] G. Montaldo, M. Tanter, J. Bercoff, N. Benech, and M. Fink, "Coherent plane-wave compounding for very high frame rate ultrasonography and transient elastography," (in eng), *IEEE Trans Ultrason Ferroelectr Freq Control*, vol. 56, no. 3, pp. 489-506, Mar 2009, doi: 10.1109/tuffc.2009.1067.
- [38] M. Capriotti, J. F. Greenleaf, and M. W. Urban, "Time-Aligned Plane Wave Compounding Methods for High-Frame-Rate Shear Wave Elastography: Experimental Validation and Performance Assessment on Tissue Phantoms," *Ultrasound Med Biol*, vol. 47, no. 7, pp. 1931-1948, Jul 2021, doi: 10.1016/j.ultrasmedbio.2021.03.003.
- [39] C. Kasai, K. Namekawa, A. Koyano, and R. Omoto, "Real-Time Two-Dimensional Blood Flow Imaging Using an Autocorrelation Technique," *IEEE Transactions on Sonics and Ultrasonics*, vol. 32, no. 3, pp. 458-464, 1985, doi: 10.1109/T-SU.1985.31615.
- [40] M. W. Urban, S. Chen, and M. Fatemi, "A Review of Shearwave Dispersion Ultrasound Vibrometry (SDUV) and its Applications," *Curr Med Imaging Rev*, vol. 8, no. 1, pp. 27-36, Feb 1 2012. [Online]. Available: <https://www.ncbi.nlm.nih.gov/pubmed/22866026>.
- [41] M. A. Kirby *et al.*, "Optical coherence elastography in ophthalmology," *J Biomed Opt*, vol. 22, no. 12, pp. 1-28, Dec 2017, doi: 10.1117/1.JBO.22.12.121720.
- [42] M. Bernal, I. Nenadic, M. W. Urban, and J. F. Greenleaf, "Material property estimation for tubes and arteries using ultrasound radiation force and analysis of propagating modes," (in English), *Journal of the Acoustical Society of America*, vol. 129, no. 3, pp. 1344-1354, Mar 2011, doi: 10.1121/1.3533735.
- [43] S. G. Chen *et al.*, "Shearwave Dispersion Ultrasound Vibrometry (SDUV) for Measuring Tissue Elasticity and Viscosity," (in English), *IEEE T Ultrason Ferr*, vol. 56, no. 1, pp. 55-62, Jan 2009, doi: 10.1109/Tuffc.2009.1005.
- [44] I. Z. Nenadic, M. W. Urban, M. Bernal, and J. F. Greenleaf, "Phase velocities and attenuations of shear, Lamb, and Rayleigh waves in plate-like tissues submerged in a fluid (L)," (in English), *Journal of the Acoustical Society of America*, vol. 130, no. 6, pp. 3549-3552, Dec 2011, doi: 10.1121/1.3654029.
- [45] "Chapter 2 - Viscoelasticity and wave propagation," in *Handbook of Geophysical Exploration: Seismic Exploration*, vol. 38, J. M. Carcione Ed.: Pergamon, 2007, pp. 51-96.
- [46] P. Kijanka, L. Vasconcelos, J. Mandrekar, and M. W. Urban, "Evaluation of Robustness of S-Transform Based Phase Velocity Estimation in Viscoelastic Phantoms and Renal Transplants," *IEEE Trans Biomed Eng*, vol. 71, no. 3, pp. 954-966, Mar 2024, doi: 10.1109/TBME.2023.3323983.
- [47] A. M. Hersh *et al.*, "Applications of elastography in operative neurosurgery: A systematic review," *J Clin Neurosci*, vol. 104, pp. 18-28, Oct 2022, doi: 10.1016/j.jocn.2022.07.019.
- [48] H. K. Lee, P. M. Holmes, J. F. Greenleaf, and M. W. Urban, "Comb Detection for Measuring Shear Wave Propagation," *IEEE Trans Ultrason Ferroelectr Freq Control*, vol. 70, no. 9, pp. 1135-1145, Sep 2023, doi: 10.1109/TUFFC.2023.3297394.

- [49] M. W. Urban, "Production of acoustic radiation force using ultrasound: methods and applications," *Expert Rev Med Devices*, vol. 15, no. 11, pp. 819-834, Nov 2018, doi: 10.1080/17434440.2018.1538782.
- [50] T. J. Czernuszewicz, C. M. Gallippi, Z. Wang, J. Ma, and X. Jiang, "Acoustic radiation force (ARF) generation with a novel dual-frequency intravascular transducer," in *2014 IEEE International Ultrasonics Symposium*, 3-6 Sept. 2014 2014, pp. 2284-2287, doi: 10.1109/ULTSYM.2014.0569.